Research Article Vol. 2, No. 2 / 15 February 2019 / OSA Continuum 332

Field demonstration of a wing-beat modulation lidar for the 3D mapping of flying insects

MARTIN JAN TAUC,[1] KURT M. FRISTRUP,[2] KEVIN S. REPASKY,[1] AND JOSEPH A SHAW[1,*]

[1] *Electrical and Computer Engineering, Montana State University, 610 Cobleigh Hall, Bozeman, MT 59715, USA*
[2] *Natural Sounds and Night Skies Division, Natural Resource Stewardship and Science, 2101 Oakridge Dr. Suite 100, Fort Collins, CO 80525, USA*
[*] *joseph.shaw@montana.edu*

Abstract: We describe a wing-beat modulation lidar system designed for the 3D mapping of flying insects in ecological or entomological studies. To better understand the signals from this instrument, we analyzed simulated signals to identify how they were affected by various imperfections, such as variations in the spacing and amplitude of each individual wing-beat reflection. In addition, a radiometric model was used to estimate signal-to-noise ratio to gain insight into the relationships between the optical system design and insect parameters (e.g., wing size, reflectivity, or diffusivity).

© 2019 Optical Society of America under the terms of the OSA Open Access Publishing Agreement

1. Introduction

In recent years, light-based methods of insect detection and classification have shown great promise for the field of entomology. Insects are both abundant and diverse and their impact on the planet and humans is of particular interest. Some studies have focused on detecting disease-carrying mosquitoes [1–6] since they are responsible for more than one million deaths each year from conditions like malaria, dengue, and West Nile virus [7,8]. Insects can also be a nuisance to farmers by ruining crops and reducing yields and this has also been a strong motivator for some studies [9–15]. On the other hand, researchers were also motivated by the fact that many insects are pollinators and a vital component for most of the world's food supply [5,10,16–20]. Finally, some studies have exploited the ability of honeybees to detect land mines through smell [21–24]. These and other studies benefit from noninvasive methods of remotely sensing insect distributions [17,25–30].

Flying insects can be sensed remotely using various optical detection methods. For example, the spectral distribution of reflected light may be useful for helping identify certain characteristics of age, sex, or species, thereby enabling detection and classification of insects [3,6,11,26,30–34]. Although this approach has shown some promise in distinguishing between different insects, the wing-beat frequency of flying insects can easily distinguish them from stationary objects, making it a good method for insect detection (although the actual wing-beat frequency can be confused by the presence of harmonics, etc.). To use the wing-beat frequency for insect classification of species and sex, the fundamental and harmonic frequencies provide a more accurate classification than the fundamental alone [2–5,9–11,16,17,22–24,29,32,33,35–37]. A combination of spectral reflectances and temporal wing-beat information provides the most robust means to classify insects; however, in this work, we exclusively focus on the wing-beat frequencies of insects as a means of detection (and not classification) against a continuously changing background.

Wing-beat frequencies have been studied through both acoustic [35,38–40] and optical means. Laboratory measurements often produce the cleanest wing-beat signals since the environment is controlled, the background is well known and constant, and the insect is confined to a volume near the beam, typically less than a few meters from the source [2–5,11,18,33,34,36,37,41,42].

#354905 https://doi.org/10.1364/OSAC.2.000332
Journal © 2019 Received 10 Dec 2018; revised 20 Dec 2018; accepted 21 Dec 2018; published 29 Jan 2019

OSA CONTINUUM

The work done in such laboratory settings has paved the way for insect detection and classification in the field by characterizing wing-beat fundamentals and harmonics for various insects, as well as interpreting the heading and orientation from the frequency information [33]. Previous remote sensing field studies have used active remote sensing systems (i.e., lidar) [9,10,16,17,21–24,28,32,43] and passive systems [28–30,44]. In general, the field studies aim to both detect and classify insects (e.g., species) along a near-horizontal path. Numerous external factors (e.g., changing background, brief transit time) cause data from field experiments to be less identifiable from laboratory experiments [16,29]. Although a highly cluttered insect signal may be too forgone to identify species, sex, or other characteristics, it is likely that it is sufficient to determine if an insect was present or not.

In this paper, we describe a wing-beat modulation lidar system designed for three-dimensional (3D) scanning and show data from a field campaign at the AMK Ranch in Grand Teton National Park, USA (43.94° N, 110.64° W) during 8 June 2016. We collected backscattered laser light in a 3D volume using an updated version of a heritage lidar system [24]. Although some studies have had 3D scanning capabilities [12,24], their intentions were not to map insects in 3D space. To our knowledge, this is the first entomological lidar to scan 3D space for insect counts based on wing-beat frequency in a general study of insects in a natural environment. During analysis, we found that many insect signals had been affected by external factors to a point where classification was impossible. As such, we performed simulations of wing-beat signals and systematically varied parameters such as peak amplitude variation and wing-beat separation time to identify their impacts on the original signal. Finally, we performed a radiometric analysis on the uncalibrated system to guide the understanding of current systems and the design of future wing-beat-modulation lidar systems. First, we describe the instrument and data processing routines; next we present experimental insect signals followed by simulated wing-beat signals; and finally we show 3D insect spatial distributions and detections as a function of time as an indication of the utility of this kind of instrument in entomological field studies.

2. Instrument description

The lidar system was adapted from a heritage system that was used for honeybee detection [22–24,45,46]. Some components from the previous system, specifically the laser, detector, and analog-to-digital converter (ADC), were implemented into the new lidar system, whereas other components, such as the telescope, lenses, filters, mirrors, and the motorized pan-and-tilt mount were newly integrated. The redesign of the wing-beat-modulation lidar system allowed for 3D scanning to map insect locations in a volume.

2.1. Hardware

The lidar system was modular in that the transmitting and receiving optics could be separated for transport or independently modified for future iterations. A schematic diagram and photograph are shown in Figs. 1 and 2. Together, the system was about 38.5 kg in mass and had a 0.5 m^2 footprint. It was attached to a pan-and-tilt mount (MOOG QPT-130) that was secured to a 1 m^2 optical breadboard for stability.

The first component in the transmitting optics was the laser head (JDS Uniphase NG-10320-100) with a pulse width of 0.6 ns, repetition rate that ranged from 4 kHz to 6 kHz (mostly dependent on temperature), laser pulse energy of 3 μJ that yielded 5 kW of pulse power, and a center wavelength of 532 nm. A small photomultiplier tube (PMT) was used to trigger the digitizer in the receiver (discussed next). Before exiting the system at the center of the receiver telescope's Ø101.6 mm central obstruction, the transmitted laser beam was expanded by a refractive telescope with 10× magnification to a size of Ø50.8 mm with half-angle beam divergence of 0.2 mrad. The total probe volume, which was constrained by the beam area and the maximum range bin, was about 0.55 m^3.

OSA CONTINUUM

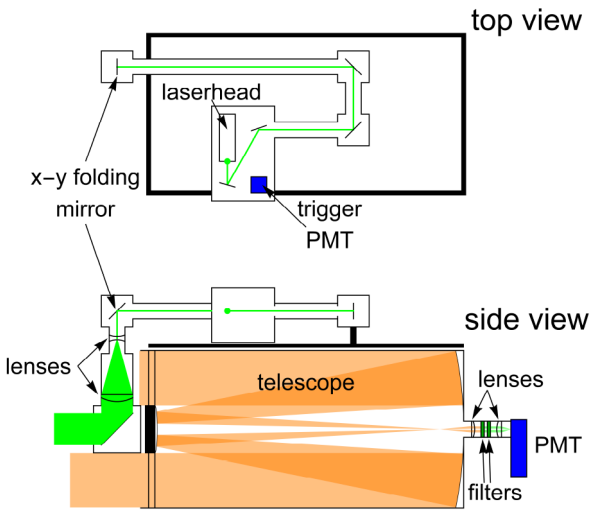

Fig. 1. Schematic of full optical setup split between the top and side view shows the beam as it expands through the transmitting optics and exits the system. The receiving optics collect, filter, and detect the return signal.

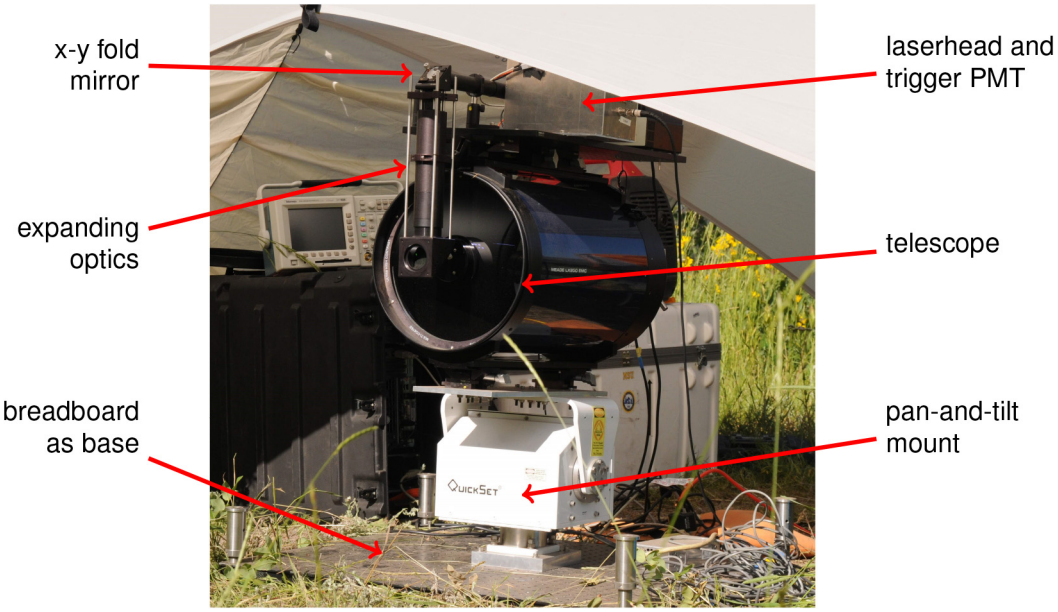

Fig. 2. Full optical setup photograph shows the lidar system during field campaign.

The first component in the receiving optics was the Schmidt-Cassegrain telescope (12" Meade LX200 Classic) with a focal length of 3048 mm, a full aperture of Ø304.8 mm, and effective (unobscured) area of 577.6 cm^2. On the back end, a short lens tube assembly housed a collimating lens (ThorLabs LA1951-A), two laser line filters (ThorLabs FL532-3) with 61.2% transmission at the center wavelength of 532 nm (optical density of 0.2) and a full width at half maximum of 3 nm. Although the filter transmits beyond 1500 nm, the detector PMT's multialkali photocathode response steeply declines at about 700 nm, so outside of the 532 nm region the optical density

OSA CONTINUUM

was about 6. Following these filters was a focusing lens (ThorLabs LA1131-A), with a 50-mm focal length that focused the beam onto a PMT (Hamamatsu H9305-04, rise time = 1.4 ns). The inclusion of the filtering optics at the back end resulted in an effective focal length of 4590 mm for the entirety of the receiving optics. Considering the rectangular effective area of the PMT, the diagonal (largest) field-of-view (FOV) was 1.5 mrad, and the horizontal (smallest) FOV was 0.4 mrad. Finally, the current from the PMT was converted to a digital number against a 50 Ω resistor on the ADC (Gage CS14200 with 14 bits, 200 megasamples per second, 100 MHz bandwidth, and RC time constant of 2 ns).

2.2. Software

Software was developed to control the hardware and to process and analyze the collected data. MATLAB was used to control the ADC card and the pan-and-tilt mount through a single script for ease of use, and to perform the post-processing routines. Although we used the algorithms from previous single-species studies of honeybees as a guide [23], the post-processing in this more general insect study was more complex, and our system was not calibrated for optical cross sections or intended to classify species or sex [16]. Furthermore, our background was frequently changing and we often observed non-insect objects, such as trees. Considering this, we manually searched the data for insect wing-beat modulation signatures.

2.2.1. Instrument control

The goal of the experiments was to count insects throughout a 3D volume as a function of time throughout the day and night in preparation for later experiments where we studied the effects of artificial light sources on insect distributions. The system would step through a series of pan and tilt coordinates (called "vectors" in this paper) and collect data. During the time that it moved from vector to vector, the software would store the data, the pan and tilt coordinates, and timestamps. Data were collected for about 0.2 s (depending on the current repetition rate of the laser), and each run (i.e., movement to a vector and data collection) lasted for a total of about 2 s. Over the course of an entire scan (typically about 9 min), 10% was spent on data collection and 90% was spent moving. The infrequency of data collection as compared to movement is likely one of the reasons the lidar did not collect as many samples as other similar systems [9,17,43].

Raw data were stored in 1024×200 (time $\times$ range) arrays, much like Hoffman et al. [23], and saved as a field in a MATLAB structure. Other important parameters, such as the pulse separation time, which ranged from 167 µs to 250 µs, were stored as separate fields within the MATLAB structure and used in the post-processing algorithms. The range resolution, limited by the sample rate and electronic bandwidth of the ADC (200 MHz and 100 MHz, respectively), was 0.75 m.

2.2.2. Post-processing

Detecting insect signatures in a large dataset was all done in post-processing. The routines, explained below, were designed to find insect signals among noise and hard-target returns. Signals that came from insect wing beats were manually identified by analyzing the amplitude and frequency of the detected signal. The process did not consider that the same insect could be counted multiple times; although, outside of a few events, most signals were separated by at least many seconds, and the infrequency of insect detection suggests that it would have been unlikely for two insects to occupy the same volume at the same time. However, counting the same insect again after multiple seconds was possible. Furthermore, in contrast with other studies that had pink noise ($1/f^{\beta}$) [16], the noise within this system was white from 5 Hz to 3000 Hz within the uncertainty in our measurements.

When detected with a wing-beat modulation lidar, flying insects produce a unique signal from static objects in the scan region. A typical scan region contained trees, rocks, and vegetation,

OSA CONTINUUM

all of which produced a lidar signal. However, the static objects produced a frequency lower than the minimum resolvable frequency of the lidar system. Even slowly moving objects, such as swaying grass, falling leaves, or other animals would also oscillate at low frequencies. Insect wings, on the other hand, oscillate up to 1 kHz [34], making them easy to distinguish.

Distinguishing insects from other objects was done by analyzing the frequency domain of each signal with a Discrete Fourier Transform (DFT, which we used because early attempts at other methods of power spectrum estimation yielded similar results). The maximum resolvable frequency was 2.5 kHz for the typical laser pulse repetition frequency of 5 kHz. Similarly, the minimum resolvable frequency (or frequency resolution) was 5 Hz, found as the inverse of the product of the number of pulses in the time-domain signal (1024) and the time spacing between pulses (0.2 ms). However, the minimum measurable wing-beat frequency is actually higher than this, limited by the insect's flight velocity and laser beam diameter. For example, an insect flying at 1 m s^{-1} perpendicular to a 50-mm-diameter beam would encounter the beam for 0.05 s, corresponding to a Nyquist-limited wing-beat frequency of 40 Hz.

The details are described below for identifying insects from the DFT, but the basic analysis was performed by identifying the fundamental frequency of a signal by inspection, and classifying it as insect based on the amplitude of the fundamental and harmonics, similar to previous studies [17,21–24,30,32,33,42]. The decisions were made by a human user who judged each data set by the amplitude and shape of the time- and frequency-domain signals. Namely, large amplitudes with well-defined spacings were accepted as insects.

Specifically, the manual three-step process identified the presence of insects in space and time. The software pre-processed the data by normalizing each array to the maximum return signal in that scan, and then a background signal (accounting for overlap and range) was determined by taking the mean of data where no insect or hard target returns were present and was subtracted from each array. In the first step of the processing routine, the user scrolled through false color images of every data array (such as the one shown in Fig. 3), and flagged it when an event

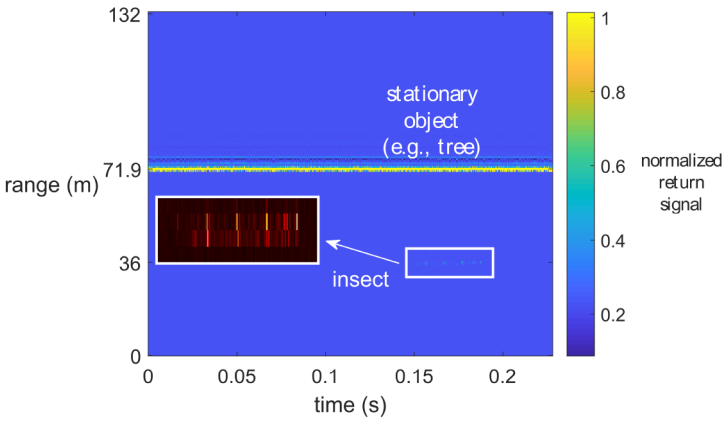

Fig. 3. Data from a field experiment show a hard target at 71.9 m and a modulated signal from 0.14 s to 0.19 s at 36.0 m that is from an insect. The insect signal is zoomed and the color changed to emphasize the modulated pattern. The 36.0 m range bin is plotted in Fig. 4.

was present. An event was defined as a brief signal with apparent oscillations. In the second step, each flagged data array was examined by the user to identify the range at which the event took place. Finally, the third step plotted the flagged range bins of each event in time, and frequency. Figures 4 and 5 are both examples of plots that the user would use to identify if the signal originated from an insect. Some signals, such as Fig. 4, had well-defined peaks in both the time and frequency domain, whereas others, such as Fig. 5, had muddled signals in both

OSA CONTINUUM

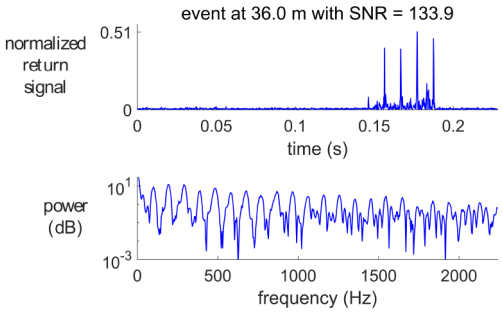

Fig. 4. The time- and frequency-domain signals for a "very likely" insect from a field campaign on 8 June 2016 show four strong and evenly spaced peaks in time and well-defined harmonics in frequency.

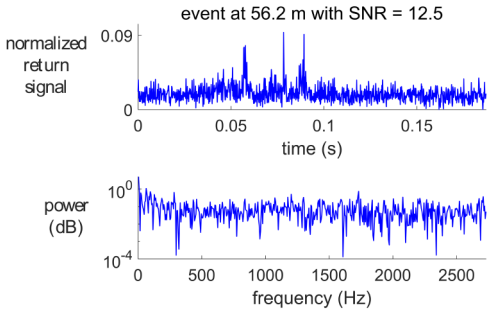

Fig. 5. The time- and frequency-domain signals for a "somewhat likely" insect measurement from a field campaign on 8 June 2016 had muddled peaks in time and no clear fundamental or harmonics in frequency.

domains. This led to a tiered classification system where the user would classify the event into "very likely" (Fig. 4), "somewhat likely" (Fig. 5), or "somewhat/very unlikely" categories. Part of the classification was based on the signal-to-noise ratio (SNR), defined as the mean of the peaks divided by the standard deviation of the non-insect signal. Although this process was open to some biasing and inconsistencies, analysis done in Sections 3.2 and 5 suggested that the classifications were probably accurate.

The "very likely" insect cases were sent through a final analysis step where their fundamental and harmonics were identified by the user. In the frequency spectrum, the signal was either represented as a single large-amplitude fundamental peak or as a series of large-amplitude harmonics. In the first case, the user would simply identify the frequency of the largest peak; however, in the other situation the user used the separation between harmonics to determine the fundamental frequency. This additional analysis on "very likely" insects returned fundamental and harmonic frequencies.

Figure 4 shows the time- and frequency-domain signals for a signal classified as "very likely," based on past work from laboratory [33,42] and field measurements [17,22–24,30,32]. The time-domain signal had very sharp peaks between 0.14 s and 0.19 s, relatively no noise floor, and slight variation in peak amplitude. The frequency domain had many well-defined harmonics spaced by 100 Hz and very little noise.

A more common signal, shown in Fig. 5, represented the case of a "somewhat likely" insect. The time-domain signal appeared to have a modulated signal between 0.05 s and 0.1 s. There was a large amount of noise in the time domain, and each peak had a different width. The

OSA CONTINUUM

frequency domain is difficult to read and extract much useful information about the wing-beat period. Nonetheless, the combination of spikes in the time domain, and a few low-power peaks at 64 Hz and 96 Hz in the frequency domain suggested that this was a "somewhat likely" insect.

In the above method, insects were detected (but not classified) based on the return signal from their oscillating wings. The basic method of identifying an insect event in space and time has been used before and is well documented for laboratory tests and some field experiments. Data collected in field campaigns are mixed with external factors that cause the wing-beat signatures to be less clear than those from laboratory measurements, causing them to have insufficient frequency information [29]. If these muddled signals were truly insects, however, then they are likely to carry important information about spatial distributions, and should thus be analyzed. Therefore, to better understand how different patterns of signal, noise, and measurement conditions affect the pure insect wing-beat signals, we modeled temporal wing-beat patterns and their frequency spectra so that we could then use the findings to infer information about an insect based on the detected signal.

3. Simulated wing-beat signals

From our experiments, we found that pure wing-beat signals are often muddled by various known and unknown factors. For example, we know shot noise and the transit time of the insect through the probe volume greatly impact our ability to identify an insect; however, we also assume that variables such as the orientation of the insect in space contribute to distortion in our signal. These factors could easily cause a clean wing-beat pattern to become nearly unrecognizable as an insect. To understand how the detected signals related back to actual wing-beat waveforms, we simulated a perfect instance and systematically added and varied different types of noise and disruptions.

3.1. Pure wing-beat signals

For the purposes of signal processing, an ideal (although non-physical) wing-beat signal was an infinite series of Dirac delta functions, more commonly referred to as a comb function, as defined by Eq. (1). To approach a more realistic scenario, we considered factors such as dwell time, partially specular wings, and noise sources from the instrument (an even more realistic simulation could include the low-frequency signal contributed by the insect body reflection). Insect speeds can greatly vary, but a reasonable estimate is about 1 m s^{-1}. Considering an insect flying at this speed perpendicular to the optical axis that passes through the Ø50.8 mm beam would result in a dwell time of about 0.05 s, and thus a minimal resolvable frequency of 40 Hz. Some insects will spend more time in the beam, whereas others will only pass through a portion of it, and so this value can vary. Dwell time is accounted for by multiplying the comb function with a rect function of that width, defined by Eq. (2). Furthermore, each Dirac delta function in the comb would have some width, since the wings are not perfectly specular; in fact wings are likely a combination of diffuse and specular components [16,21,29,32,34]. To account for some diffusivity, the delta functions were convolved with a narrow gauss function, as defined by Eq. (3).

$$\mathrm{comb}\left(\frac{t}{T}\right) = T\sum_{k=-\infty}^{\infty}\delta\left(\frac{t}{T}-k\right) \tag{1}$$

$$\mathrm{rect}\left(\frac{t}{U}\right) = \begin{cases} 0 & \text{if } \left|\frac{t}{U}\right| > \frac{1}{2} \\ 1 & \text{if } \left|\frac{t}{U}\right| \le \frac{1}{2} \end{cases} \tag{2}$$

$$\mathrm{gauss}\left(\frac{t}{\sigma}\right) = \exp\left(-\frac{1}{2}\left(\frac{t}{\sigma}\right)^2\right) \tag{3}$$

The product of the comb and rect convolved with the gauss function represented the exemplar insect wing-beat for signal processing. The time- and frequency-domain signals are shown in

OSA CONTINUUM

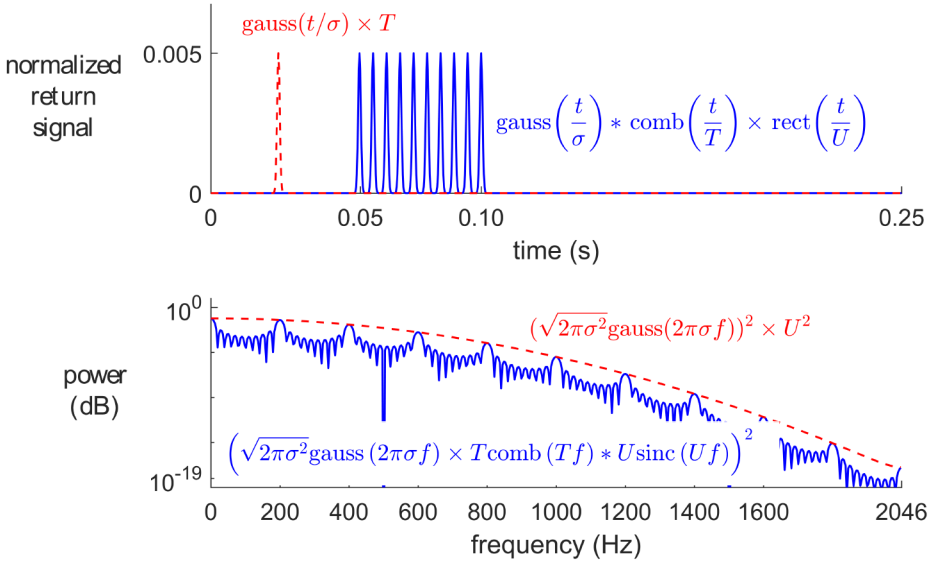

Fig. 6. The exemplar insect was simulated in the time domain (top) and the Fourier transformed signal represented the frequency domain (bottom). In the time domain, the red dashed line represents the gauss function that a windowed comb was convolved with for width (note that it is multiplied by T in order to view the two functions on the same scale). In the frequency domain, the gauss function widens and windows the fundamental and harmonics (note that it has been multiplied by U^2 so that it can be viewed on the same scale).

Eq. (4) and Fig. 6.

$$\mathscr{F}\left\{\text{gauss}\left(\frac{t}{\sigma}\right) * \text{comb}\left(\frac{t}{T}\right) \times \text{rect}\left(\frac{t}{U}\right)\right\} = \sqrt{2\pi\sigma^2}\text{gauss}(2\pi\sigma f) \times T\,\text{comb}(Tf) * U\,\text{sinc}(Uf) \quad (4)$$

The different functions in the time domain had important effects in the frequency domain. The width of the time window (rect) inversely determined the width of the peaks in the frequency domain, such that if an insect spent more time within the beam, the frequency domain would have harmonics with narrow profiles. Similarly, the width of the Gaussian determined the number of harmonics in the frequency domain. If an insect were to produce very narrow (almost delta-like) peaks, then a large number of harmonics would be present in the frequency domain. Since no disruptions of any kind were present in these simulations, they were very unrealistic, but they gave us insight as to what an undisturbed signal looked like.

3.2. *Noisy wing-beat signals*

A more realistic example of a detected signal had a variety of noise or other disruptions. We simulated four different types of disruptions and inspected their Fourier transforms for the case of a varying peak amplitude, sigma (σ) jitter (i.e., variation in width of each wing reflection), time jitter (i.e., variation in time between each wing reflection), and a noise floor (i.e., instrument noise and background fluctuations). Each individual contribution and all contributions together are represented in Fig. 7. Red dotted lines are included in the frequency domain to identify where the exemplar insect would have the first six harmonics.

Each different contribution had a unique impact on the frequency-domain signal when compared to the exemplar insect (Fig. 6). We do not specifically attribute a particular cause for each effect, but rather assume that multiple imperfections can culminate to cause any of the distortions.

OSA CONTINUUM

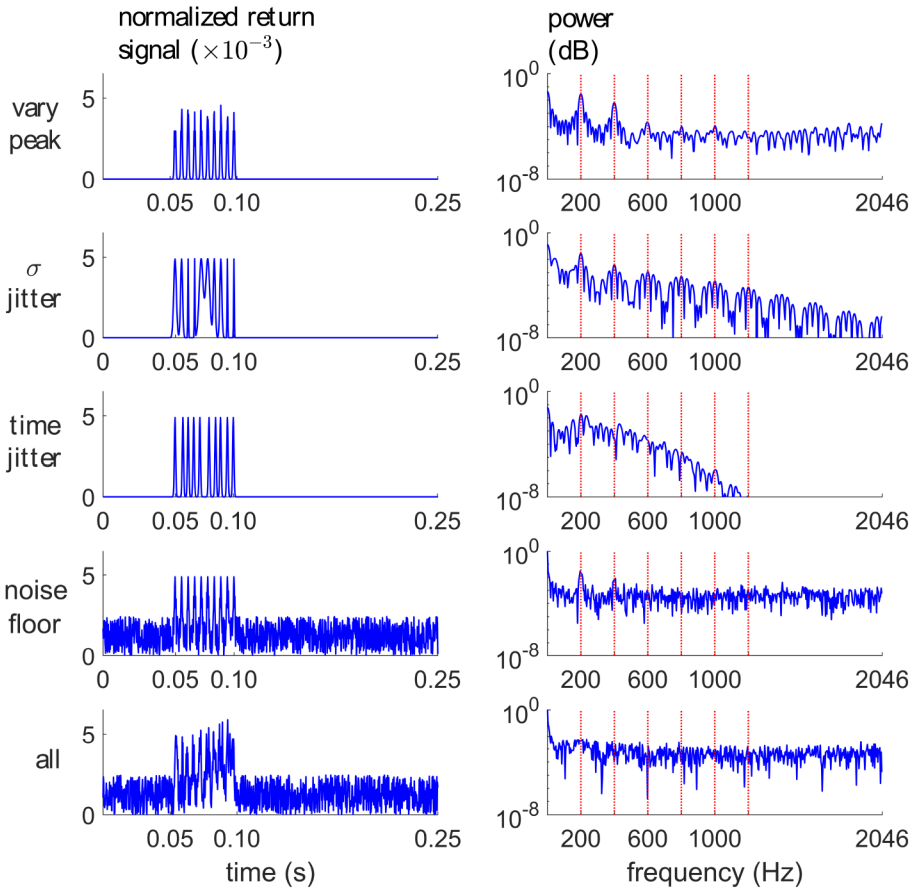

Fig. 7. Simulations showing the time and frequency domains for an exemplar insect wing-beat signal that has been disrupted by four different factors show how each contribution in the time domain affects the frequency domain. Peak amplitude variation increased the overall power of higher frequencies, but reduced the amplitude of harmonics. σ jitter modified the local shape of all harmonics. Time jitter distorted the fundamental and reduced the amplitude of higher frequencies. A noise floor produced more noise in the frequency domain and reduced signal past the second harmonic. The combination of each contribution produced a frequency spectrum from which a frequency could not be identified easily.

The addition of peak amplitude variation reduced the amplitude of higher harmonics, but also increased the overall amplitude at higher frequencies. Sigma (σ) jitter caused the local regions around the higher harmonics to increase in amplitude. The addition of time jitter reduced higher frequencies and made the fundamental tone nearly unreadable. Finally, the noise floor reduced the readability of the frequency domain, especially after the second harmonic, and greatly reduced the amplitude of the first and second harmonics. Although these four contributions are only a subset of all possible disturbances, they likely represent some of the most common disruptions. In fact, the "all noise" case looks similar to Fig. 5, suggesting that this particular event was probably an insect. Since "very likely" insect signals are very clean, we believe that most of the disturbances modeled above come from the way that the insect flies through the beam; it is likely that the orientation changes, or the heading shifts while the insect is within the beam. It is also possible that the laser stability limits contribute to the signal fluctuation over realistic averaging times.

OSA CONTINUUM

4. Radiometric analysis

The simulated wing-beat signals from Section 3 are helpful when interpreting important information about the insect, such as the wing-beat frequency or perhaps its orientation in space, since that can have an impact on harmonics [33]. Similarly, a radiometric analysis provides insight to how the size and reflectivity of the wings or other instrument design parameters influence the signal detectability. In this section, we first present radiometric calculations leading to SNR and then illustrate how the simulated signals vary with experimental or design parameters.

4.1. Modeling return signals

The transmitted signal began at the laser and ended at the insect. The return signal began with the insect wing and terminated on the PMT. We calculated the final optical power as a function of the various components within the lidar system and experimental settings. The laser quantities, mirror reflectivities, and lens transmissions were determined from manufacturer data sheets; atmospheric attenuation was modeled using the MODTRAN radiative transfer code; and some unknown quantities, such as the diffusivity of the insect wing, were assumed.

The assumptions we made were based on some real signals that we detected, but such parameters must be modified for a reader's particular experiment because many of the parameters can vary greatly. Wing reflectivities in the visible spectrum, for example, can vary from a few percent [21,31,33] to above 70% for some butterflies and beetles [47,48]. Based on the worst-case signal from Fig. 5, we assumed a very low wing reflectivity of 1% and very small effective wing size (i.e., area of near-specular reflection) of 0.1 mm^2, and scattering into a projected solid angle of $\pi/10$ sr, which could vary a lot based on the wing curvature and sensing geometry [21], as well as other factors such as species, age, or sex of the insect [32,49]. We use the projected solid angle into which light from the wing is scattered (Ω_{scat}) as means to approximate the bidirectional reflectance distribution function (BRDF); a more rigorous treatment would use a full BRDF approach, but since we did not know this quantity for all the insects in this study, we adopted this approximation. We also assumed that the laser beam quality was affected by atmospheric turbulence, and so we use an effective divergence angle (α) to account for this. These assumptions are reiterated and carried out through the calculations below. To begin with, the laser power (Φ_{laser}) was determined as the ratio of the laser pulse energy ($Q_{laser} = 3\,\mu$J) and pulse width ($\Delta t_{laser} = 0.6$ ns, which was assumed to be flat). The detected flux (Φ_{det}) was reduced from the original laser power by optical elements, atmospheric attenuation, and scattering properties of the insect wing. Specifically, the mirrors at 45° and slant angles ($\rho_{mir45} = 99.4\%$ and $\rho_{mir8} = 99.6\%$, respectively), lenses ($\tau_{lens} = 99.5\%$), and the atmosphere ($\tau_{atm} = 98.3\%$) affected the outgoing beam. The effective divergence half angle ($\alpha = 0.4$ mrad) of the 10× expanded laser, the distance from the lidar system to the insect ($d_{ins} = 56.2$ m), and the initial diameter of the beam as it exited the system ($D_{beam} = 0.0508$ m) influenced the irradiance on the wing. The wing itself had an effective size ($A_{wing} = 0.1\ mm^2$) based on the region from which the near-specular light reflected, a reflectivity ($\rho_{wing} = 1\%$), and a diffusivity ($\Omega_{scat} = \pi/10$ sr). Finally, the transmittances and reflectivities of the receiving optics were considered. This included the effective aperture of the telescope ($A_{Teff} = 577.6\ cm^2$), which accounted for the obstructions from the secondary mirror and lens tube assembly, the transmittance of the Schmidt plate ($\tau_T = 98\%$) and laser line filters ($\tau_{filt} = 61.2\%$) as well as the final focusing and collimating lenses ($\tau_{lens} = 99.5\%$) and the reflectivity of the primary and secondary mirrors ($\rho_T = 94\%$). These were applied to calculate the detected power.

$$\Phi_{det} = \frac{\Phi_{laser}\rho_{mir8}\rho_{mir45}^{5}\tau_{lens}^{4}\tau_{atm}^{2}\rho_{wing}\tau_T\tau_{filt}^{2}\rho_T^{2}A_{Teff}A_{wing}}{\pi d_{ins}^{4}(tan(\alpha)+\frac{D_{beam}}{2})^{2}\Omega_{scat}} = 0.012\,\mu W \tag{5}$$

OSA CONTINUUM

The PMT detector had a quantum efficiency ($\eta_{pmt} = 0.163$) at its peak wavelength of $\lambda = 532$ nm. Also, assuming typical daytime conditions, we calculated that the background (Φ_{bg}) produced about 0.05 µW of optical power. By taking into account the charge of an electron (q), Planck's constant (h), the speed of light (c), and the PMT's dark current ($i_d = 1$ nA), the cathode current (i_c) was

$$i_c = \frac{\eta_{pmt} q(\Phi_{det} + \Phi_{bg})\lambda}{hc} + i_d = 5.3\,\text{nA}. \tag{6}$$

Finally, the detector was shot noise limited, so for PMT gain G, the SNR was determined by

$$SNR = \frac{Gi_c}{\sigma_{shot}} = \frac{Gi_c}{\sqrt{2qG^2 i_c \Delta f}} = 10.4, \tag{7}$$

where Δ_f, the electrical bandwidth of the ADC, was 100 MHz.

4.2. Signal dependence on experimental parameters

There is a trade between the achievable *SNR* and size (and cost) of the lidar instrument. We used the radiometric analysis as a design tool, such as aiding in the selection of a telescope aperture (see Fig. 8), and also to interpret the return signal. The reflectivity, size, and specular or diffusive properties of the wing, and the divergence angle of the outgoing beam are typically different for every detected event. By making some assumptions, such as the size and reflectivity of an insect wing based on the species in the area and time of day, and taking into account the range bin where the insect was detected, other information like the diffusivity of the wing potentially could be interpreted. The relationship between these variables, the SNR, and the range to the insect are described below.

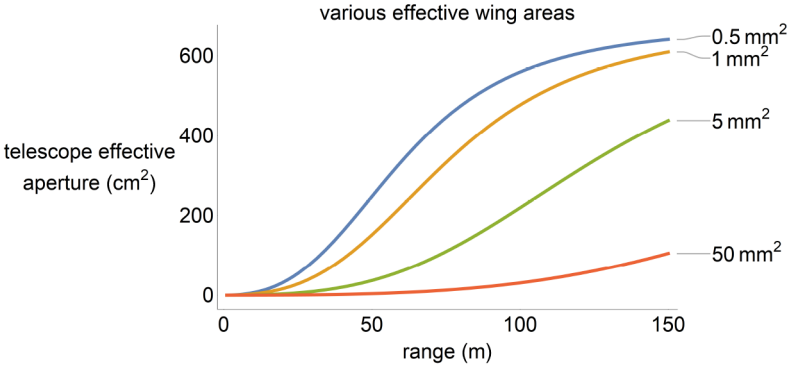

Fig. 8. A plot of telescope effective aperture necessary to detect different effective sizes of insect wings at various ranges with an SNR of 10 can provide valuable insight into what telescope is needed depending on the requirements of the entomological research. In these simulations, the reflectivity was 1% and light from the wing scattered into $\pi/10$ sr, and the divergence half angle of the outgoing laser was 0.4 mrad.

In design stages of the lidar system, the radiometric analysis provided useful insight into the selection of components. For a lowest allowable SNR value (in our case 10), a variety of telescope sizes were considered. Figure 8 plots the telescope effective aperture as a function of range to the insect for different effective wing sizes and a fixed SNR = 10. By inspection of this figure, a lidar system could detect an insect with a wing area of 5 mm^2 at a range of 100 m with SNR = 10 if a telescope had an effective aperture of at least 200 cm^2. If the design required that we detect smaller wing sizes at 100 m and the same SNR, then the system would need a larger telescope for our selected laser. This was not the only consideration when choosing a

OSA CONTINUUM

telescope, but it certainly was an important aspect when choosing a major part of the receiver optics. Similarly, Fig. 9 shows curves of wing reflection area that produce SNR = 10 at ranges up to 150 m for five different values of wing reflectivity.

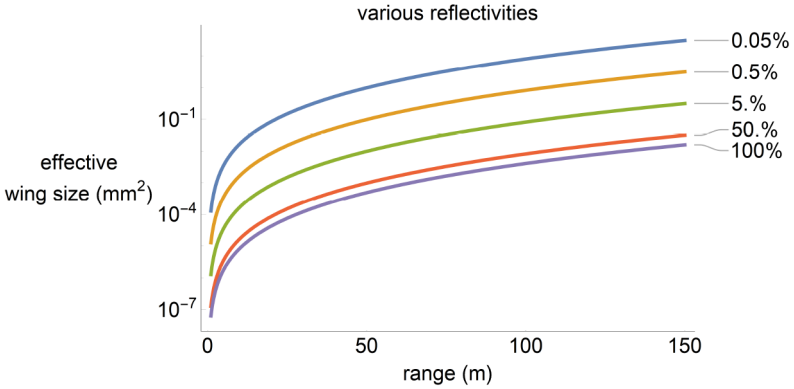

Fig. 9. The necessary effective wing size to acquire an SNR of 10 for various partially specular (i.e., $\Omega_{scat} = \pi/10$ sr) reflectivity values. The effective telescope aperture area was 577.6 cm^2 and the laser divergence half angle was 0.4 mrad.

The goal of this insect lidar was to detect insects in a field as proof of concept for entomological and ecological studies. The type of insects that we could detect came down to the scattering medium: the insect wing. As long as the wing had the right combination of size, reflectivity, and diffusivity, the receiving optics would be able to detect it. Furthermore, entomologists may be able to use this information to suggest whether the insect was male or female, old or young, or what species it was. The diffusive and spectral properties of some wings, for example, change over a lifetime [6,33]. Figures 8 and 9 are just two examples of how Eq. (5) can be manipulated to hone in on a specific parameter.

5. Spatial and temporal insect distributions

Mapping insects in 3D space within their natural environment using a lidar system, to our knowledge, has not been done prior to this study. The scanning capability of the lidar system can provide insight into insect movement over time. One particular area of interest is how insects respond to variables like noise and light. For example, Kirkeby et al. [17] pointed a stationary entomological lidar near a light trap and observed light-dependent insect behavior. In a similar way, a 3D scanning lidar system can map insect distributions from more dimensions. The added spatial information likely carries important information. One application of this method is to improve the understanding of light pollution on insects, and how future methods of lighting could then mitigate these affects.

As discussed in Section 2, detected insects were classified into two categories, “very likely” and “somewhat likely.” In Section 3, our simulations showed that good wing-beat signals can be quickly distorted by various contributions, suggesting that the “somewhat likely” insects are almost certainly insects. In Fig. 10, histograms of “very likely” and “somewhat likely” insects are plotted as a function of time during the course of the day. The pattern of “very likely” insects follows results from other studies [9,10,17], in that insects become more abundant around dusk (and dawn, although this is not shown here since we did not collect data at that time). Although our data do not continue much past sunset, they do agree with other studies [9,17] in that the greatest number of insect counts occur just after sunset. Furthermore, the pattern is present in both the “very likely” and “somewhat likely” insect cases, suggesting that the “somewhat likely” insects are indeed insects since they follow the same pattern.

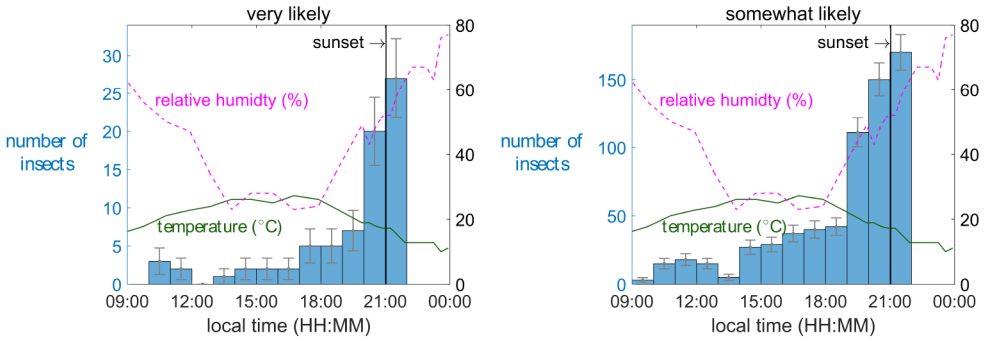

Fig. 10. Histograms of insect counts for "very likely" (left) and "somewhat likely" (right) show very similar trends suggesting that even "somewhat likely" insects are indeed insects. The blue bars correspond to the left axis and indicate the number of insects during that one-hour bin. Error bars assume that the insect counts follow a Poisson distribution. The relative humidity (pink dashed line) and temperature (green line) correspond to the right axis (measured at the Jackson Hole Airport about 38 km from the lidar site with wind speeds varying up to 6.3 m s^{-1}). Sunset is represented by the black line around 21:00.

Arbitrary pan and tilt positioning of the mount allows for 3D mapping of insect locations. For brevity, we do not report range-dependent insect counts from this preliminary experiment; however, a sense of insect distributions within the measured volume is shown in Fig. 11(a). The

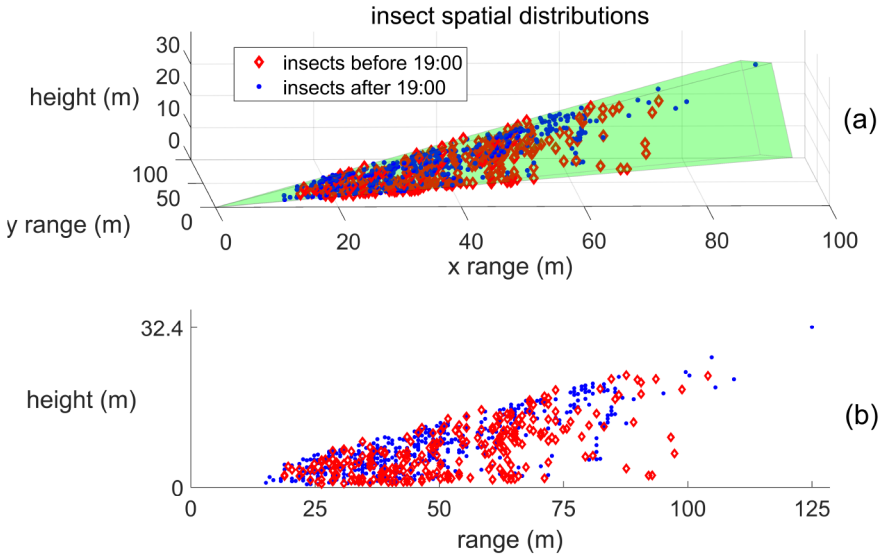

Fig. 11. Mapping insect spatial distributions in 3D space was possible due to the pan and tilt capability of the lidar instrument. In (a), the green region represents the scanning volume, red triangles represent insect counts before 19:00 (local time) and blue dots represent insect counts after 19:00. The intent of this particular figure is to show that capability of the 3D mapping, not necessarily to identify any trends. In (b), the 3D distributions are projected onto the range-height plane.

green volume represents the scan region, the blue dots represent insects after 19:00 local time, whereas the red diamonds represent insects detected before 19:00. According to Fig. 10, insects are most abundant after 19:00, and so we plotted 3D insect distributions with this time difference

OSA CONTINUUM

color coded. To help the reader interpret this densely packed 3D plot, Fig. 11(b) shows the same insect distribution as a range-height profile. The data set plotted here included 738 insects detected in a time period of approximately 12 hours. The greatest insect-detection range in this case was 125 m at a height near 32.4 m, although we note that dense forest below this height was one reason more insects were not detected at such long ranges. This type of data can be used to design future experiments involving placement of variable light and noise sources within the scan region for monitoring how the insects react. For example, if a light source were placed into the scan region at 19:00, the before and after distributions are likely to be very different.

An important characteristic about the scanning lidar system is its unreliability in counting absolute insect number. Insect counting, essentially a Poisson process, can be made most useful by taking relative measurements, rather than absolute ones. Therefore, some dependencies are not considered here. For example, fewer insects will be counted in a region of partial overlap, and smaller insects will be counted close to the lidar although they may not reflect enough light to be detected at large ranges; large insects, on the other hand, may be detected at larger range due to their size. Such dependencies would need to be taken into account if the user was interested in knowing insect size as a function of range, or similar parameters. For the purposes of our study, however, we were not considering such dependencies.

6. Conclusion

The instrument described in this paper was upgraded from a heritage system originally developed at Montana State University for land mine detection using honeybees [21–24,45]. Since the latest iteration, we have improved hardware and software so that the instrument is capable of detecting a variety of insects, and not just honeybees. The most significant improvement was the pan-and-tilt mount, which allowed the system to point in any arbitrary direction without sacrificing beam quality or accounting for different field-of-view overlaps as a function of pointing vector. The software was also generalized for broad insect detection by incorporating the entire available frequency spectrum and not just the range around 200 Hz. Although other lidar systems have detected insects out to 1 km [28], our instrument did not sample past about 130 m. Nonetheless, our radiometric analysis indicates that our setup could detect an insect at that range, as long as the insect had a large wing size and reflectivity.

Detecting insects in their natural environment without disruption can provide valuable information to entomologists. To locate flying insects in a 3D volume, we designed, built, and implemented a lidar system for field studies. During a field campaign in Grand Teton National Park, we detected a few hundred insects, but found their signals to vary greatly in terms of noise, peak intensity and spacing, and other factors. In order to better understand these signals, we simulated pure wing-beat signatures and added noise and other disturbances to observe the effects in the time and frequency domains. Furthermore, we performed a radiometric analysis to guide us in the development of the lidar system, and to interpret some information about insect signals, such as the effective reflecting area of the insect wing.

Many studies seek to classify an insect in species, sex, or other characteristic, but our study was only focused on insect detection. Some events detected by the lidar system were unclassifiable; however, based on the fact that insect signals degrade, those events can at least be counted as insect events. Although insect classification can lead to deeper analysis, detecting insects in 3D space is still an important parameter in many studies.

Because the lidar system was upgraded from a heritage system, some components were not ideal for insect studies. For example, a short-wave infrared laser wavelength would have yielded a larger reflectivity from insects, is eye-safe at higher powers, and does not disrupt the insects [2,3,26,43]. Furthermore, a lidar system could provide additional information about insect behavior with modifications that could include a quadrant camera for information about insect flight path [28–30,33,34], polarization capabilities for wing and body contributions [1,3,21], and

OSA CONTINUUM

multiple wavelength channels for assessment of biological tissue, such as melanin [3,26,30,32,44]. The simulations and radiometric analysis presented in this paper are another tool in the arsenal of detecting and classifying insects. Further, while the real insect signals from the 3D-mapping entomological lidar provide little information into the type of insect, they add a new dimension to previous works. Considering these steps, the future version of this lidar system will be able to detect insect responses to different variables, including those needed to test insects' response to noise and light pollutants.

Funding

National Park Service (NPS) (Task Agreement P15AC01807).

Acknowledgments

This work was partially supported by a housing subsidy from the University of Wyoming-National Park Service Research Station (http://uwnps.org). We also thank the staff at Towne's Harvest Garden (Montana State University) for letting us test our instrument near their beehives.

References

1. S. Jansson, P. Atkinson, R. Ignell, and M. Brydegaard, "First polarimetric investigation of malaria mosquitoes as lidar targets," IEEE J. Sel. Top. Quantum Electron. **25**(1), 1–8 (2019).
2. A. P. Genoud, R. Basistyy, G. M. Williams, and B. P. Thomas, "Optical remote sensing for monitoring flying mosquitoes, gender identification and discussion on species identification," Appl. Phys. B: Lasers Opt. **124**(3), 46 (2018).
3. A. Gebru, S. Jansson, R. Ignell, C. Kirkeby, J. C. Prangsma, and M. Brydegaard, "Multiband modulation spectroscopy for the determination of sex and species of mosquitoes in flight," J. Biophoton. **11**(8), e201800014 (2018).
4. I. Potamitis and I. Rigakis, "Measuring the fundamental frequency and the harmonic properties of the wingbeat of a large number of mosquitoes in flight using 2D optoacoustic sensors," Appl. Acoust. **109**, 54–60 (2016).
5. G. E. A. P. A. Batista, Y. Hao, E. Keogh, and A. Mafra-Neto, "Towards automatic classification on flying insects using inexpensive sensors," in *Proceedings – 10th International Conference on Machine Learning and Applications, ICMLA 2011*, vol. 1 (2011), pp. 364–369.
6. V. S. Mayagaya, K. Michel, M. Q. Benedict, G. F. Killeen, R. A. Wirtz, H. M. Ferguson, and F. E. Dowell, "Non-destructive determination of age and species of Anopheles gambiae s.l. using near-infrared spectroscopy," Am. J. Trop. Medicine Hyg. **81**(4), 622–630 (2009).
7. H. Caraballo and K. King, "Emergency department management of mosquito-borne illness: malaria, dengue, and West Nile virus," Emerg. Medicine Pract. **16**, 1–24 (2014).
8. World Health Organization, *Global technical strategy for malaria, 2016-2030* (WHO Press, World Health Organization, 20 Avenue Appia, 1211 Geneva 27, Switzerland (www.who.int), 2015).
9. E. Malmqvist, S. Jansson, S. Zhu, W. Li, K. Svanberg, S. Svanberg, J. Rydell, Z. Song, J. Bood, M. Brydegaard, and S. Åkesson, "The bat–bird–bug battle: Daily flight activity of insects and their predators over a rice field revealed by high-resolution scheimpflug lidar," R. Soc. Open Sci. **5**(4), 172303 (2018).
10. S. Zhu, E. Malmqvist, W. Li, S. Jansson, Y. Li, Z. Duan, K. Svanberg, H. Feng, Z. Song, G. Zhao, M. Brydegaard, and S. Svanberg, "Insect abundance over Chinese rice fields in relation to environmental parameters, studied with a polarization-sensitive CW near-IR lidar system," Appl. Phys. B: Lasers Opt. **123**(7), 211 (2017).
11. Y. Y. Li, H. Zhang, Z. Duan, M. Lian, G. Y. Zhao, X. H. Sun, J. D. Hu, L. N. Gao, H. Q. Feng, and S. Svanberg, "Optical characterization of agricultural pest insects: a methodological study in the spectral and time domains," Appl. Phys. B: Lasers Opt. **122**(8), 213 (2016).
12. L. Mei, Z. G. Guan, H. J. Zhou, J. Lv, Z. R. Zhu, J. A. Cheng, F. J. Chen, C. Löfstedt, S. Svanberg, and G. Somesfalean, "Agricultural pest monitoring using fluorescence lidar techniques: feasibility study," Appl. Phys. B: Lasers Opt. **106**(3), 733–740 (2012).
13. R. Aljaryian and L. Kumar, "Changing global risk of invading greenbug Schizaphis graminum under climate change," Crop Prot. **88**, 137–148 (2016).
14. R. J. C. Cannon, "The implications of predicted climate change for insect pests in the UK, with emphasis on non-indigenous species," Glob. Chang. Biol. **4**(7), 785–796 (1998).
15. M. P. Zalucki, A. Shabbir, R. Silva, D. Adamson, L. Shu-Sheng, and M. J. Furlong, "Estimating the economic cost of one of the world's major insect pests, plutella xylostella (lepidoptera: plutellidae): just how long is a piece of string?" J. Econ. Entomol. **105**(4), 1115–1129 (2012).
16. E. Malmqvist, S. Jansson, S. Torok, and M. Brydegaard, "Effective parameterization of laser radar observations of atmospheric fauna," IEEE J. Sel. Top. Quantum Electron. **22**(3), 327–334 (2016).

OSA CONTINUUM

17. C. Kirkeby, M. Wellenreuther, and M. Brydegaard, "Observations of movement dynamics of flying insects using high resolution lidar," Sci. Rep. **6**(1), 29083 (2016).
18. J. van Roy, J. De Baerdemaeker, W. Saeys, and B. De Ketelaere, "Optical identification of bumblebee species: effect of morphology on wingbeat frequency," Comput. Electron. Agric. **109**, 94–100 (2014).
19. S. G. Potts, J. C. Biesmeijer, C. Kremen, P. Neumann, O. Schweiger, and W. E. Kunin, "Global pollinator declines: trends, impacts and drivers," Trends Ecol. Evol. **25**(6), 345–353 (2010).
20. R. Dirzo, H. S. Young, M. Galetti, G. Ceballos, N. J. Isaac, and B. Collen, "Defaunation in the anthropocene," Science **345**(6195), 401–406 (2014).
21. J. A. Shaw, N. Seldomridge, D. Dunkle, P. Nugent, L. Spangler, J. Bromenshenk, C. Henderson, J. Churnside, and J. Wilson, "Polarization lidar measurements of honey bees in flight for locating land mines," Opt. Express **13**(15), 5853–5863 (2005).
22. K. S. Repasky, J. A. Shaw, R. Scheppele, C. Melton, J. L. Carlsten, and L. H. Spangler, "Optical detection of honeybees by use of wing-beat modulation of scattered laser light for locating explosives and land mines," Appl. Opt. **45**(8), 1839–1843 (2006).
23. D. S. Hoffman, A. R. Nehrir, K. S. Repasky, J. A. Shaw, and J. L. Carlsten, "Range-resolved optical detection of honeybees by use of wing-beat modulation of scattered light for locating land mines," Appl. Opt. **46**(15), 3007–3012 (2007).
24. E. S. Carlsten, G. R. Wicks, K. S. Repasky, J. L. Carlsten, J. J. Bromenshenk, and C. B. Henderson, "Field demonstration of a scanning lidar and detection algorithm for spatially mapping honeybees for biological detection of land mines," Appl. Opt. **50**(14), 2112–2123 (2011).
25. Z. Guan, M. Brydegaard, P. Lundin, M. Wellenreuther, A. Runemark, E. I. Svensson, and S. Svanberg, "Insect monitoring with fluorescence lidar techniques: field experiments," Appl. Opt. **49**(27), 5133–5142 (2010).
26. M. Brydegaard, "Advantages of shortwave infrared LIDAR entomology," in *Imaging and Applied Optics 2014,* (OSA, Washington, D.C., 2014), p. LW2D.6.
27. M. Brydegaard, Z. Guan, M. Wellenreuther, and S. Svanberg, "Insect monitoring with fluorescence lidar techniques: feasibility study," Appl. Opt. **48**(30), 5668 (2009).
28. M. Brydegaard, A. Merdasa, A. Gebru, H. Jayaweera, and S. Svanberg, "Realistic instrumentation platform for active and passive optical remote sensing," Appl. Spectrosc. **70**(2), 372–385 (2016).
29. S. Jansson and M. Brydegaard, "Passive kHz lidar for the quantification of insect activity and dispersal," Animal Biotelemetry **6**(1), 6 (2018).
30. A. Gebru, E. Rohwer, P. Neethling, and M. Brydegaard, "Investigation of atmospheric insect wing-beat frequencies and iridescence features using a multispectral kHz remote detection system," J. Appl. Remote. Sens. **8**(1), 083503 (2014).
31. D. G. Stavenga, H. L. Leertouwer, and B. D. Wilts, "Coloration principles of nymphaline butterflies – thin films: melanin, ommochromes and wing scale stacking," J. Exp. Biol. **217**(12), 2171–2180 (2014).
32. M. Brydegaard, A. Gebru, and S. Svanberg, "Super resolution laser radar with blinking atmospheric particles — application to interacting flying insects," Prog. Electromagn. Res. **147**, 141–151 (2014).
33. M. Brydegaard, "Towards quantitative optical cross sections in entomological laser radar – potential of temporal and spherical parameterizations for identifying atmospheric fauna," PLoS One **10**(8), e0135231 (2015).
34. M. Brydegaard, S. Jansson, M. Schulz, and A. Runemark, "Can the narrow red bands of dragonflies be used to perceive wing interference patterns?" Ecol. Evol. **8**(11), 5369–5384 (2018).
35. T. Ganchev and I. Potamitis, "Automatic acoustic identification of singing insects," Bioacoustics **16**(3), 281–328 (2007).
36. A. Moore and R. H. Miller, "Automated identification of optically sensed aphid (homoptera: aphidae) wingbeat waveforms," Annals Entomol. Soc. Am. **95**(1), 1–8 (2002).
37. Y. Chen, A. Why, G. Batista, A. Mafra-Neto, and E. Keogh, "Flying insect classification with inexpensive sensors," J. Insect Behav. **27**(5), 657–677 (2014).
38. R. W. Mankin, D. W. Hagstrum, M. T. Smith, a. L. Roda, and M. T. K. Kairo, "Perspective and promise: a century of insect acoustic detection and monitoring," Am. Entomol. **57**(1), 30–44 (2011).
39. D. R. Reynolds and J. R. Riley, "Remote-sensing, telemetric and computer-based technologies for investigating insect movement: A survey of existing and potential techniques," Comput. Electron. Agric. **35**(2–3), 271–307 (2002).
40. R. W. Mankin, "Acoustical detection of aedes taeniorhynchus swarms and emergence exoduses in remote salt marshes," J. Am. Mosquito Control. Assoc. **10**, 302–308 (1994).
41. D. M. Unwin and C. P. Ellington, "An optical tachometer for measurement of the wing-beat frequency of free-flying insects," J. Exp. Biol. **82**, 377–378 (1979).
42. G. Batista, E. Keogh, A. M. Neto, and E. Rowton, "SIGKDD demo: sensors and software to allow computational entomology, an emerging application of data mining," in *17th ACM SIGKDD international conference on Knowledge discovery and data mining – KDD '11*, (2011), pp. 761–764.
43. M. Brydegaard, A. Gebru, C. Kirkeby, S. Åkesson, and H. Smith, "Daily evolution of the insect biomass spectrum in an agricultural landscape accessed with lidar," in *EPJ Web of Conferences*, vol. 119 B. Gross, F. Moshary, and M. Arend, eds. (EDP Sciences, 2016), p. 22004.

OSA CONTINUUM

44. A. K. Gebru, M. Brydegaard, E. Rohwer, and P. Neethling, "Probing insect backscatter cross-section and melanization using kHz optical remote detection system," in *Remote Sensing and Modeling of Ecosystems for Sustainability XIII*, vol. 9975 W. Gao and N.-B Chang, eds. (International Society for Optics and Photonics, 2016), p. 997504.
45. J. A. Shaw, K. S. Repasky, J. L. Carlsten, L. H. Spangler, and D. S. Hoffman, "Optical detection of oscillating targets using modulation of scattered laser light," (2009).
46. M. J. Tauc, K. M. Fristrup, and J. A. Shaw, "Development of a wing-beat-modulation scanning lidar system for insect studies," in *Lidar Remote Sensing for Environmental Monitoring 2017*, vol. 10406 U. N. Singh, ed. (SPIE, 2017), p. 104060G.
47. M. Burresi, L. Cortese, L. Pattelli, M. Kolle, P. Vukusic, D. S. Wiersma, U. Steiner, and S. Vignolini, "Bright-white beetle scales optimise multiple scattering of light," Sci. Rep. **4**(1), 6075 (2014).
48. P. Vukusic and J. R. Sambles, "Shedding light on butterfly wings," in *Physics, Theory, and Applications of Periodic Structures in Optics*, vol. 4438 P. Lalanne, ed. (International Society for Optics and Photonics, 2001), p. 85.
49. E. I. Svensson, F. Eroukhmanoff, K. Karlsson, A. Runemark, and A. Brodin, "A role for learning in population divergence of mate preferences," Evolution **64**(11), 3101–3113 (2010).

130.131.66.118 {ts '2019-06-18 14:11:50'}